Zeitschrift für Kristallographie

International Journal for Structural, Physical, and Chemical Aspects of Crystalline Materials

Volume 208 1993

R. Oldenbourg Verlag · München

Index of Volume 208 (1993)

Part I

B. B. Zvyagin, D. Yu. Pushcharovsky
The modular analysis of Ca_2SiO_4-$Ca(OH)_2$-$Ca_4Si_3O_{10}$ structures . . . 1

A. Allescher-Last, A. Czybulka, H.-U. Schuster
Neue ternäre Phasen in den Systemen Seltene Erden-Lithium-Zinn . . 11

H. Möller, Th. Kellersohn, M. Schmidt, H. D. Lutz, J. K. Cockcroft
Structure refinement of $BaCl_2 \cdot D_2O$ and $SrCl_2 \cdot D_2O$ by neutron powder diffraction 19

N. N. Hoang, F. Valach, M. Melník
Structure of bis(salicylato)di(nicotinamide)copper(II) 27

P. Wu, J. A. Ibers
Synthesis and structure of $Ba_2LaAg_5S_6$ and $Ba_2YAg_5S_6$ 35

S. B. Bellad, A. M. Babu, M. A. Sridhar, A. Indira, M. S. Madhava, J. Shashidhara Prasad
Crystal structure of mesogenic material – 2-(4′-cyano phenyl)-5-n-heptyl-1,3 dioxane 43

A. M. Babu, S. B. Bellad, M. A. Sridhar, A. Indira, M. S. Madhava, J. Shashidhara Prasad
Crystal structure of mesogenic material – 4′-n-pentyl cyclohexyl-(4-n-pentyl cyclohexane)-1-carboxylate 49

F. Demartin, T. Pilati, H. D. Gay, C. M. Gramaccioli
The crystal structure of a mineral related to paulkerrite 57

H. L. Meyerheim, I. K. Robinson, V. Jahns, P. J. Eng, W. Moritz
Coverage dependent adsorption sites in the K/Cu(100) system: A crystal truncation rod analysis 73

New Crystal Structures

K.-J. Range, A. Gietl, U. Klement, K. G. Lange
Crystal structure of thulium oxide sulfide (2/2/1), Tm_2O_2S 95

K.-J. Range, F. Rau, U. Klement
Crystal structure of thulium sulfide (5/7), Tm_5S_7 97

R. Kempe, J. Sieler, E. Hintzsche, W. Schroth
Crystal structure of 3′-mercapto-7,7,7′,7′-tetramethyl-2,2′[bi]bicyclo-[2.2.1]heptylidene-3-thione, $C_{20}H_{29}S_2$ 99

U. Klement
Crystal structure of 3-bromo-2,6-dimethoxy-N,N-dimethylthiobenzamide, $(C_6H_2)Br(OCH_3)_2CSN(CH_3)_2$ 102

V. Langer, H.-D. Becker
Crystal structure of "C_2-symmetric" head-to-tail photodimer of 9-(2-hydroxy-2-propyl)anthracene, $C_{34}H_{32}O_2$ 104

V. Langer, H.-D. Becker
Crystal structure of centrosymmetric head-to-tail photodimer of 9-(2-hydroxy-2-propyl)anthracene, $C_{34}H_{32}O_2$ 108

U. Klement
Crystal structure of pentacarbonyl-pyridine-tungsten (0), $W(CO)_5$-(NC_5H_5) 111

U. Klement
Crystal structure of pentacarbonyl-4-methyl-pyridine-tungsten(0), $W(CO)_5(NC_5H_4)CH_3$ 114

A. Heiske, P. Zugenmaier
Crystal structure of 4-(4-hydroxy-1-butoxy)-4′hydroxybiphenyl (H4HBP), $C_{16}H_{18}O_3$ 116

A. Heiske, P. Zugenmaier
Crystal structure of 4-(6-hydroxy-1-hexoxy)-4′-hydroxybiphenyl (H6HBP), $C_{18}H_{22}O_3$ 119

P. G. Jones, A. K. Fischer
Crystal structure of 4,5-dichloro-5-ethyl-6-methyl-2-methoxy-2-oxo-5,6-dihydro-2H-oxaphosphorine, $C_8H_{13}Cl_2O_3P$ 123

P. G. Jones, E. Bembenek
Crystal structure of (tetrahydrothiophene)-trichlorogold(III), $C_4H_8AuCl_3S$ 126

P. G. Jones, A. Weinkauf
Crystal structure of p-fluorobenzenesulphonamide, $C_6H_6FNO_2S$ . . . 128

P. G. Jones, J. Lautner
Crystal structure of (diphenylsulphide)trichlorogold(III), $C_{12}H_{10}AuCl_3S$ 130

P. G. Jones, A. Chrapkowski, P. Boldt, J. Rase
Crystal structure of 2-methyl-5-phenyltriazolo[4,5-d]-triazole, $C_9H_8N_6$. 133

P. G. Jones, P. Bubenitschek, H. Hopf, Z. Pechlivanidis
Crystal structure of 4-acetyl[2.2]paracyclophane, $C_{18}H_{18}O$ 136

P. G. Jones, P. Boldt, S. Zippel
Crystal structure of 1-amino-4-(4-methoxy-phenoxy)-anthraquinone-(9,10), $C_{21}H_{15}NO_4$ 139

U. Flörke, H.-J. Haupt
Crystal structure of N-[2,2-bis(diphenylphosphino)ethyl]-N′,N′-dimethyl-1,3-propanediamine-P,P′-tetracarbonylchromium, $(CO)_4Cr(P(C_6H_5)_2)_2(C_2H_3)(NHC_3H_6N(CH_3)_2)$ 142

R. Kempe, J. Sieler, E. Hintzsche, W. Schroth
Crystal structure of bis-(4,4′,5,5′-tetramethyl-thieno)[3,2-c;2′,3′-e]-1,2-dithiin, $C_{12}H_{12}S_4$ 145

R. Kempe, M. Pink, E. Hintzsche, W. Schroth
Crystal structure of bis-thieno[3,2-c;2′,3′-e]-1,2-dithiin, $C_8H_4S_4$ 148

M. Pink, R. Kempe, E. Hintzsche
Crystal structure of 2,3,4,5,10,11,12,13-octamethyl-1,6,7,8,9,14,15,16-octathia-tetracyclopenta [a,c,g,i] cyclododecene, $C_{24}H_{24}S_8$ 151

S. Hormuth, H.-U. Reißig, S. Foro, H. J. Lindner
Crystal structure of (5R,1S′)-5-[1-(N,N-dibenzyl-amino)ethyl]-2(3H)-4,5-dihydrofuranone, $CH(CH_2)_2COOCHCH_3NCH_2(C_6H_5)CH_2(C_6H_5)$ 154

S. Hormuth, H.-U. Reißig, S. Foro, H. J. Lindner
Crystal structure of (2S,1′S)-2-[1-(N,N-dibenzyl-amino)ethyl]-3(2H)-4,5-dihydrofuranone, $OCH_2CH_2COCHCH(CH_3)NCH_2(C_6H_5)CH_2$-$(C_6H_5)$ 157

U. Klement
Crystal structure of exo-6-methoxy-1-(4-pyridyl)-1a,2,3,7b-tetrahydro-1H-cyclopropa[a]naphthalene, $CH_3O(C_{10}H_9)CH(C_5H_4N)$ 161

R. Boese, D. Bläser, D. Oster, H. Weber
Crystal structure of 1-(2,4-dinitrophenyl)-3-methyl-1H-cycloheptapyrazol-6-one, $C_{15}H_{10}N_4O_5$ 164

Part II

H. L. De Bondt, N. M. Blaton, O. M. Peeters, C. J. De Ranter
Calculation of electrostatic potentials from multipole charge densities 167

R. K. Arni, V. C. A. Martins, Y. P. Mascarenhas, G. Goissis, C. A. Kavounis
The crystal structure of 1-(N^a-trifluoracetylalanyl)-indoline 175

K. A. Al-Farhan
Crystal structure of triphenylphosphine oxide oxalic acide benzene . . 181

J. Kusz, H. Böhm
Incommensurate/commensurate phase transition of $NbTe_4$ 187

H. Haeuseler
Materials with layered structures IX. The structure of $(Mn_{0.6}Ti_{0.4})(Ga_{1.6}Mn_{0.4})S_4$ 195

A. J. C. Wilson
Laue and Patterson symmetry in the complex case. 199

L. Walz, D. Thiery, E.-M. Peters, H. Wendel, E. Schönherr, M. Wojnowski
Crystal structure of GeI_4 at 100 K and 297 K 207

P. G. Jones, E. Bembenek
Redetermination of the structure of tetrakis(acetonitrilo)silver(I) perchlorate at 173 K 213

Short Communications

S. A. Kim, C. Griewatsch, H. Küppers
Optical activity in potassium trihydrogen di(*cis*-4-cyclohexene-1,2-dicarboxylate) dihydrate (point group $\bar{4}2m$) 219

K. Peters, E.-M. Peters, H. G. von Schnering, G. Bringmann, D. Leimkötter
Crystal structure of 2*S*,4*S*-2,4-carboxymethyl-5,5-dimethyl-1,3-thiazolidine 223

New Crystal Structures

R. Kempe, J. Sieler, E. Hintzsche, W. Schroth
Crystal structure of (1s)-4,7,11,11,12,12-hexamethyl-1,2,3,4,7,8,9,10-octahydro-1r,4c;7t,10t-dimethano-dibenzoc[c;e]-1,2,3-trithiepin, $C_{20}H_{28}S_3$ 229

R. Kempe, J. Sieler, E. Hintzsche, W. Schroth
Crystal structure of bi-(7,7,7′,7′-tetramethyl 2,2′[bi]bicyclo[2.2.1]-heptylidenyl-3-thione)-3′,3′-disulfide, $C_{40}H_{56}S_4$ 232

J. Pécaut, J. P. Lévy
Crystal structure of ter(2-amino-5-nitropyridinium) hexachloroindate, $(C_5H_6N_3O_6)_3(InCl_6)$ 235

J. Pécaut
Crystal structure of dimethylaminopyridinium-L-monohydrogentartrate dihydrate, $(C_7H_9N_3O_2)(C_4H_6O_6)(H_2O)_2$ 238

J. Pécaut, R. Masse
Crystal structure of dimethylammonium stilbazolium-N-hydroxide bis-(dihydrogenphosphate)(trihydrogenphosphate) dihydrate, $(C_{15}H_{18}N_2O)(H_2PO_4)_2(H_3PO_4)(H_2O)_2$ 241

A. Kowalski
Crystal structure of potassium salt of 4,5-dinitroimidazole, $KC_3N_2H(NO_2)_2$ 244

Y. Fukuda, F. W. Lichtenthaler, H. J. Lindner, I. Svoboda
Crystal structure of 5R,7S,9S,10-tetrahydroxy-7,9-di-O-isopropylidene-8S-methyl-3-methoxy-dec-2Z-enoic acid 1,5-lactone, $(C_4H_3O_2)(CH_3)_2(CH_2OH)(CH_3)(CH_2)(C_5H_4O)OO(CH_3)$ 246

A. Alvarez-Larena, J. F. Piniella, N. Arnau, M. Moreno-Mañas, R. Pleixats
Crystal structure of trans-(benzenethiolato)-chlorobis(triphenylphosphine)palladium(II), $Pd(SC_6H_5)(P(C_6H_5)_3)_2Cl$ 249

K. Eckardt, I. Svoboda, I. Pabst
Crystal structure of dimethylammoniumtrichlorocuprate, $(CH_3)_2NH_2(CuCl_3)$ 253

Y. Le Fur, J. Pécaut, J. P. Lévy
Crystal structure of bis(4-methoxypyridine-N-oxide)dichlorocopper, $(C_6NO_2H_7)_2(CuCl_2)$ 255

M. T. Averbuch-Pouchot
Crystal structure of 3-ammonium propionic acid monohydrogen-phosphite, $(H_3NC_2H_4COOH)(HPO_3H)$ 257

G. Valle, M. Crisma, M. Pantano, F. Formaggio, C. Toniolo, J. Kamphuis
Crystal structure of oxazol-5(4H)-one from N^{α}-para-bromobenzoyl-C^{α}-methyl-D-leucyl-C^{α}-methyl-D-leucyl-C^{α}-methyl-D-leucine, $C_{28}H_{32}BrN_3O_4$ 259

M. Hušák, B. Kratochvíl, A. Jegorov, P. Bulej
Crystal structure of 7-(1-hydroxy-1,2,2-trimethylpropyl)-6,14-etheno-6,7,8,14-tetrahydrothebaine, thevinol, $C_{27}H_{37}NO_4$ 263

P. Bulej, A. Jegorov, J. Novotný, M. Hušák, B. Kratochvíl
Crystal structure of 17-cyano-7-(1-hydroxy-1,2,2-trimethylpropyl)-6,14-etheno-6,7,8,14-tetrahydro-17-northebaine, cyanothevinol, $C_{27}H_{34}N_2O_4$ 266

J. Ondracek, S. Pakhomova, M. Hovorka, R. Scigel
Crystal structure of 6′-tert-butyl-2,2′-dihydroxy-1,1′-binaphthalene-3-carboxylate clathrate with acetone, $(C_{24}H_{25}O_4)_3C_3H_6O$ 269

J. Wunderle, J. Scholz, E. Hovestreydt
Crystal structure of 1-(4-methyl-phenyl)-3-methyl-4-phenyl-1-aza-1,3-butadiene, $C_{17}H_{17}N$ 274

J. Wunderle, J. Scholz, R. Fröhlich
Crystal structure of 1,2,3,4-tetraphenyl-1,4-diaza-1,3-butadiene, $C_{26}H_{20}N_2$ 277

U. Klement
Crystal structure of N-[2,2,2-trifluoro-1-(4′-hydroxyphenyl)ethyl]-N-phenyl-benzamide, $(C_6H_5)CN(C_6H_5)OCH(CF_3)(C_6H_4OH)$ 280

U. Klement
Crystal structure of exo-1-(4-pyridyl)-1a,2,3,7b-tetrahydro-1H-cyclopropa[a]naphthalene, $(C_{10}H_{10})CH(C_5H_4N)$ 283

U. Klement
Crystal structure of neodymium tetracyanopalladate(II) 12-hydrate, $Nd_2(Pd(CN)_4)_3(H_2O)_{12}$ 285

U. Klement
Crystal structure of europium tetracyanopalladate(II) 12-hydrate, $Eu_2(Pd(CN)_4)_3(H_2O)_{12}$ 288

A. C. Stückl, U. Klement, K.-J. Range
Crystal structure of (biphenylato-C2,C2')-(bipyridine-N,N')palladium(II), $(C_{12}H_8)Pd(C_{10}N_2H_8)$ 291

A. C. Stückl, U. Klement, K.-J. Range
Crystal structure of (biphenylato-C2,C2')-((4,4'-dichloro)bipyridine-N,N')platinum(II), $(C_{12}H_8)Pt(C_{10}H_6N_2Cl_2)$ 294

A. C. Stückl, U. Klement, K.-J. Range
Crystal structure of chloro(diethylsulfido)-((2'-thienyl)pyridinato-N,C3') platinum(II), $PtClS(C_2H_5)_2(C_5H_4N)(C_4H_2S)$ 297

U. Klement
Crystal structure of di-μ-chloro-bis(2-phenylpyridinato-C2,N'-palladium(II)), $((C_{11}H_8N)PdCl)_2$ 299

A. C. Stückl, U. Klement, K.-J. Range
Crystal structure of (biphenylato-C2,C2')-((4,4'-dimethyl)bipyridine-N,N')platinum(II) dichloromethane, $(C_{12}H_8)Pt(C_{10}H_6N_2(CH_3)_2)CH_2Cl_2$ 302

M. Geselle, H. Paulus, I. Pabst
Crystal structure of trimethylammonium triiodomercurate, $(CH_3)_3NHHgI_3$ 305

U. Englert, P. Paetzold, E. Eversheim
Crystal structure of bis(diisopropylamino)-phosphine azide, $((C_3H_7)_2N)_2P(N_3)$ 307

S. Eichhorn, S. Foro, H. Neunhoeffer, H. J. Lindner
Crystal structure of 4,5,6-tris(dimethylamino)-1,2,3-triazine, $(N_3C_3)N(CH_3)_2N(CH_3)_2N(CH_3)_2$ 310

S. F. Lincoln, I. B. Mahadevan, E. R. T. Tiekink, A. D. Ward
Crystal structure of 4-methyl-N-(2-methyl-6-methoxy-8-quinolyl)benzenesulphonamide, $C_{18}H_{18}N_2O_3S$ 313

James A. Ibers
Crystal structure of tetraethylammonium perchlorate, $N(C_2H_5)_4ClO_4$ 316

P. R. Brooks, R. Bishop, J. A. Counter, E. R. T. Tiekink
Crystal structure of anti-(Z)-bisfenchylidene, $C_{20}H_{32}$ 319

F. Weller, D. Nusshär, K. Dehnicke
Crystal structure of bis(triphenylphosphane)-iminium chloride, toluene adduct, $(C_6H_5)_3PNP(C_6H_5)_3Cl(C_7H_8)_{0.5}$ 322

S. Buth, B. Neumüller, K. Dehnicke
Crystal structure of tetraphenylphosphonium tetrachloro-oxo-tetrahydrofurane-tungstate(V), $P(C_6H_5)_4(WOCl_4(OC_4H_8))$ 326

U. Flörke, H.-J. Haupt
Crystal structure of di-μ-methylphenylphosphanido-bis(tetracarbonylrhenium), $(P(CH_3)(C_6H_5))_2(Re(CO)_4)_2$ 330

U. Flörke, H.-J. Haupt
Crystal structure of di-μ-ethylphenylphosphanido-bis(tetracarbonylrhenium), $(P(C_2H_5)(C_6H_5))_2(Re(CO)_4)_2$ 332

L. Párkányi, S. Sharma, F. Cervantes-Lee, K. H. Pannell
Crystal structure of μ-oxo-bis(chlorohafnocene), $((C_5H_5)_2HfCl)_2O$ . . 335

F. Knoch, R. Appel, W. Paulen
Crystal structure of 1,2,3-tri-tert-butyl-1,2,3-triphosphetan-4-one, $((CH_3)_3C)_3P_3CO$ 338

P. G. Jones
Crystal structure of 1,8-diphthaliso-imidonaphthalene, $C_{26}H_{14}N_2O_4$ 341

P. G. Jones
Crystal structure of hetisinone hydrate, $C_{20}H_{27}NO_4$ 344

P. G. Jones
Crystal structure of tetra-*n*-butylammonium bis(pentafluorophenyl)-gold(I), $C_{28}H_{36}AuF_{10}N$ 347

P. G. Jones, P. Bubenitschek, W. Grahn, D. Remmers
Crystal structure of 4-(Z-α,β-dichlorvinyl)-7-methyl-[2.2]paracyclophane, $C_{19}H_{18}Cl_2$ 351

P. G. Jones, J. Lautner, C. Thöne
Crystal structure of (μ-p-chlorophenylselenolato)-bis(triphenylphosphinegold(I)) hexafluoroantimonate, $ClC_6H_4Se(AuP(C_6H_5)_3)_2(SbF_6)$ 354

P. G. Jones
Crystal structure of 1,4-dimethyl-2,3-diphenyl-1,4,3,2-diazadiphospholidin-5-one-2-oxide, $C_{15}H_{16}N_2O_2P_2$ 358

P. G. Jones
Crystal structure of tetra-*n*-butylammonium trans-dichlorobis(pentafluorophenyl)aurate(III), $(C_4H_9)_4N(Cl_2Au(C_6F_5)_2)$ 362

M. T. Averbuch-Pouchot
Crystal structure of 2-butylammonium monohydrogen-phosphite, $(H_3NC_4H_9)(HPO_3H)$ 366

H. G. von Schnering, W. May, K. Peters
Crystal structure of dodecachlorooctahedro-hexamolybdenum, Mo_6Cl_{12} 368

G. Meyer, D. J. Hinz, U. Flörke
Crystal structure of caesium titanium tribromide, $CsTiBr_3$ 370

M. Tillard-Charbonnel, A. Chahine, C. Belin
Crystal structure of sodium silver gallium (36/7/73), $Na_{36}Ag_7Ga_{73}$ . . 372

A. Olbertz, D. Stachel, I. Svoboda, H. Fueß
Crystal structure of cobalt ultraphosphate, CoP_4O_{11} 374

P. Sondergeld, H. Paulus, H. Fueß
Crystal structure of ammonium triiodocadmate monohydrate, $NH_4CdI_3(H_2O)$ 376

H.-J. Deiseroth, H. Pfeifer
Crystal structure of germanium tetraindium tetrasulfide, $GeIn_4S_4$ and germanium tetraindium tetraselenide, $GeIn_4Se_4$ 378

J. M. Kalychak, V. I. Zaremba, P. Y. Zavalij
Crystal structure of holmium cobalt indium (6/2/1), $Ho_6Co_{2+x}In_{1-x}$, $x = 0.135$ 380

P. Ugliengo, D. Viterbo, G. Chiari
Erratum: 207, 9–23 (1993), MOLDRAW: Molecular graphics on a personal computer 383

Errata zum Supplement Issue No. 7, 10.–12. März 1993 in Bochum . 385

Invitation to the 15th European Crystallographic Meeting 387

Author Index of Volume 208 389

Subject Index of Volume 208 393

Formulae Index of Volume 208 393

Zeitschrift für Kristallographie 208, 73–92 (1993)

Coverage dependent adsorption sites in the K/Cu(100) system: A crystal truncation rod analysis

H. L. Meyerheim, I. K. Robinson*, V. Jahns, P. J. Eng* and W. Moritz

Institut für Kristallographie und Mineralogie der Universität München, Theresienstr. 41, D-80333 München, Germany

Received August 8, 1992; in revised form December 8, 1992

Crystal truncation rod / Fourfold hollow site / On-top site / Surface structure

Abstract. The analysis of the intensity along the diffraction rods normal to the crystal surface (crystal truncation rods) has been used to analyse the adsorption sites of potassium atoms adsorbed at $T = 330$ K on atomically clean Cu(100) under ultra high vacuum conditions. At potassium coverages below about $\Theta = 0.18$ ML (1 ML = 1.53×10^{15} atoms cm^{-2}), where no ordered adsorbate superstructure forms, the potassium atoms are adsorbed in the fourfold hollow sites of the Cu(100) substrate at $d_\perp = 2.1(4)$ Å above the first Cu layer corresponding to an effective potassium radius of $r_{\text{eff}} = 1.5(3)$ Å which is close to the ionic radius of 1.33 Å. Within about 1–2% the substrate interlayer spacings, d_{12} and d_{23} are not affected.

At high coverage ($\Theta \approx 0.30$ ML) where an ordered incommensurate overlayer forms, the adsorption site is partially on-top. These results are in correspondence with the model of alkalimetal adsorption on metals supposing extensive charge transfer from potassium to the substrate at low coverage.

I. Introduction

Alkali metal (AM) adsorption has been of interest for long time from both, theoretical and experimental point of view (Bonzel, Bradshaw and Ertl, 1989).

* Department of Physics, University of Illinois, Urbana IL 61801, USA.

This can be understood since AM adsorption on metals represents a prototype chemisorption system and alkali metals play an important role as promoters in heterogenous catalysis.

One prominent feature of alkali metal adsorption is the rapid decrease of the substrate work function at low coverages and its subsequent increase giving rise to the characteristic minimum which is known since the 1920's (Langmuir and Kingdon, 1923).

Correspondingly a huge amount of spectroscopic and theoretical work has been performed in order to develop a consistent model which correlates the evolution of the structural and electronic properties with increasing alkali coverage.

Many studies using spectroscopic methods appear to confirm the model that an alkali metal adsorbed on a metal at low coverages, $\Theta < 0.18$ monolayers (ML) (1 ML corresponds to 1 K atom per surface Cu atom, i.e. 1 ML $= 1.53 \times 10^{15}$ K atoms/cm^2), transfers its valence electron to the substrate (Aruga, Tochihara and Murata, 1986; Soukiassan, Riwan, Lecante, Wimmer, Chubb and Freeman, 1985; Horn, Hohlfeld, Somers, Lindner, Hollins and Bradshaw, 1988; Woratschek, Sesselmann, Küppers, Ertl and Haberland, 1985; Wallden, 1985). This suggests the picture of (partially) ionic adatoms which are randomly dispersed on the surface due to electrostatic repulsion. At higher coverage, between $\Theta = 0.20$ and $\Theta = 0.30 - 0.35$ ML, the latter corresponding to the formation of about one complete overlayer, the overlap of the wave functions between neighboring alkali atoms becomes more extensive and the cohesive interaction surpasses the interaction with the substrate. In this coverage regime back donation of charge to the adatoms takes place leading to a change of the bonding character from ionic to metallic. For the system K/Cu(100) the beginning of the two dimensional condensation of the overlayer at about 0.2 ML nearly coincides with the minimum of the work function (Aruga, Tochihara and Murata, 1986).

However, the assumption that the bonding is largely ionic at coverages below $\Theta = 0.20$ ML is subject to considerable current controversy. Some experimental and theoretical studies have been interpreted to support the picture of covalent bonding at all coverages (Riffe, Wertheim and Citrin, 1990; Ishida, 1988, 1990).

Additional informations about the bonding character can be obtained by the analysis of the geometric structure. However, precise structural data are rare. The structure analysis employing the analysis of low energy electron diffraction (LEED) data is complicated by multiple scattering effects. Additionally, one complication may arise by the increased contamination rate of the surface induced by the electron beam or by electron stimulated desorption. In the present investigation the stability of the superstructure was found to be considerably shorter (about 20 min) when under observation using LEED as compared to the observation using X-rays

(about 40 min to 1 h). Consequently, studies of the adsorbate geometry have not played the central role in discussions of the nature of the adsorption mechanism and comparatively few quantitative determinations of the adatom geometry have been carried out. Thus theoretical models of AM adsorption have almost by default assumed that the adsorption position is a hollow site. It has been recently discovered that this is not always true. For the $p(2\times 2)$ phase formed by Cs/Ru(0001) (Over, Bludau, Skottke-Klein, Ertl, Moritz and Campbell, 1992), Cs/Cu(111) (Lindgren, Wallden, Rundgren, Westrin and Neve, 1983) and K/Ni(111) (Fisher, Chandavarkar, Collins, Diehl, Kaukasoina and Lindroos, 1992) on-top adsorption of the alkali atom was determined. For Cs/Ru(0001) a change to the hcp-threefold hollow position is observed at higher coverage. Using surface extended X-ray absorption fine structure (SEXAFS) measurements, probing the local order, a substitutional adsorption mechanism was determined for Na on Al(111) in the coverage regime between 0.16 ML and 0.33 ML (Schmalz, Aminpirooz, Becker, Haase, Neugebauer and Scheffler, 1991).

These examples demonstrate the importance of a detailed structural investigation and their relation to the spectroscopic results. During the last decade surface sensitive X-ray diffraction has become an important tool for the investigation of surface structures since the data analysis is based on the kinematical scattering theory (Feidenhans'l, 1989; Robinson, 1991) and powerful synchrotron X-ray sources have become available.

In this paper we present an X-ray structure analysis of submonolayers of potassium adsorbed on an atomically clean Cu(100) surface under ultra high vacuum (UHV) conditions. We have chosen this system since it represents a prototype AM/metal adsorbate system that has been investigated using electron energy loss spectroscopy (EELS), work function measurements and LEED (Aruga, Tochihara and Murata, 1984 , 1985, 1986).

Using LEED Aruga, Tochihara and Murata (1985) suggested a continuous transition between two commensurate phases labeled C1 and C2, which correspond to theoretical coverages of $\Theta = 0.30$ ML and $\Theta = 0.33$ ML, respectively. However, informations about the relative arrangement between substrate and overlayer is lacking.

Further, nothing is known about the adsorption site at coverages below about $\Theta = 0.20$ ML, where the potassium atoms do not form an ordered overlayer structure. Moreover, it is within this low coverage regime where the rapid decrease of the substrate work function is observed which is ascribed to the charge transfer from K to the Cu substrate. Consequently, in order to obtain a better understanding of the physical mechanism underlying the observed effect it is of crucial importance to investigate the atomic structure of the adsorbate system in this regime.

In this paper we show that at low coverages the potassium atoms occupy fourfold hollow sites of the Cu(100) substrate surface. At high coverages ($\Theta \approx 0.30$ ML) the adsorbate site is found to be preferentially on-top. The

structure analysis is based on the interference between the amplitudes scattered by the substrate crystal and the adsorbed layer. This allows the analysis of the local geometry of the adsorbate atoms relative to the substrate.

The next section outlines the basic principles of the structure determination using the analysis of the intensity variation along integer order reciprocal lattice rods normal to the sample surface. Section III and section IV discuss experimental details and the data analysis. The results of the structure analysis are summarized in section V in the context with the general physics of alkali adsorption. Section VI provides a short summary.

II. Analysis of crystal truncation rods

Since the early days of the X-ray scattering theory (Laue, 1936) it is well known that the finite size of the crystal gives rise to a diffuse intensity between the Bragg points. If we consider a crystal consisting of an infinite number of unit cells along the a- and b-direction (summation from $n_{1,2} = -\infty$ to $n_{1,2} = \infty$) and which is semiinfinite along the c-direction (summation from $n_3 = -\infty$ to $n_3 = 0$) the intensity distribution in reciprocal space is given by a two dimensional δ-function (in plane) and a diffuse rod normal to the sample surface (c^* direction). The scattered amplitude can be written as:

$$I_{hkl} = |F_{hkl}|^2 \cdot \left| \sum_{n_1=-\infty}^{\infty} \sum_{n_2=-\infty}^{\infty} \sum_{n_3=-\infty}^{0} e^{i2\pi(hn_1 + kn_2 + ln_3)} \right|^2 \tag{1}$$

where F_{hkl} represents the structure factor of the unit cell. The variable n_3 indicates that the structure is non periodic along the direction normal to the sample surface. If we assume all unit cells to be equal we obtain for the intensity in the limit of negligible absorption:

$$I = |F_{hkl}|^2 g(h) g(k) \frac{1}{4\sin^2 \pi l} \tag{2}$$

In Eq. (2) $g(h)$ and $g(k)$ are the Laue functions $[\sin^2(n\pi h)/\sin^2(\pi h)]$ which correspond to delta functions in the limit $n \to \infty$. Normal to the sample surface there is a diffuse rod of intensity. It is called crystal truncation rod (CTR), since it arises due to the termination of the crystal. The Miller index l is a continuous parameter. The reciprocal lattice is schematically outlined in Fig. 1, where we have plotted the intensity distribution in an **a*-c***-section. The width of the rods schematically indicates the intensity variation along **c*** which is given by Eq. (2). For convenience we use the primitive setting of the (100) surface unit cell corresponding to the tetragonal setting of the bulk unit cell. The transformations between the Miller indices related

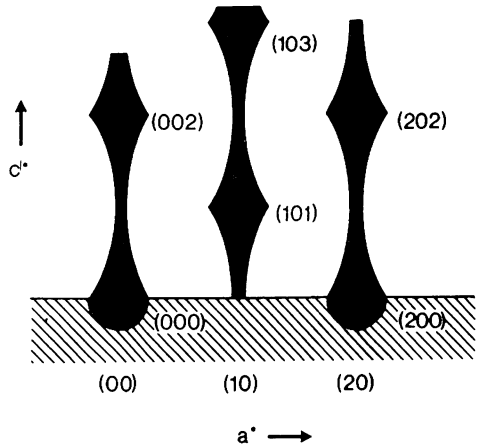

Fig. 1. Schematic drawing of the reciprocal lattice of the Cu substrate crystal in the **a*** – **c*** section showing the crystal truncation rods normal to the sample surface. The rods are present due to the termination of the crystal. The width of the rods schematically indicates the intensity variation. Bulk reflections are indexed in the tetragonal setting of the crystal (see text).

to the cubic (c) and the tetragonal (t) setting are $(11l)_c = (10l)_t$ and $(22l)_c = (20l)_t$.

Close to the Bragg peak there is a q^{-2} intensity dependence that is the result of the dynamical theory as well (Batterman and Cole, 1964) which ab initio includes the sample surface as boundary condition. The Eq. (2) neglects the effect of absorption and extinction which smooth out the singularity at the Bragg-peaks. We do not use the regime near the Bragg-peaks since it contains only information about the bulk substrate crystal.

Surface sensitivity in CTR analysis can only be achieved far off the Bragg-peaks where the substrate layers do not scatter in phase and the total scattering amplitude is in the same order of magnitude as the scattering amplitude of one adsorbate monolayer.

The Eq. (2) assumes the crystal surface to be completely flat which can be expressed by a step function, whose Fourier Transform gives the q^{-2} intensity dependence (Andrews and Cowley, 1985). However, crystal surfaces exhibit a surface roughness that leads to a steeper intensity dependence since the step function in r-space is smeared out. Robinson (1986) has developed an atomistic roughness model assuming a geometric distribution of layer occupancies, where the layer occupancy is 1.0 for layer 0, layer 1 has a fraction of β occupied sites, layer 2 has a fraction of β^2 and so on.

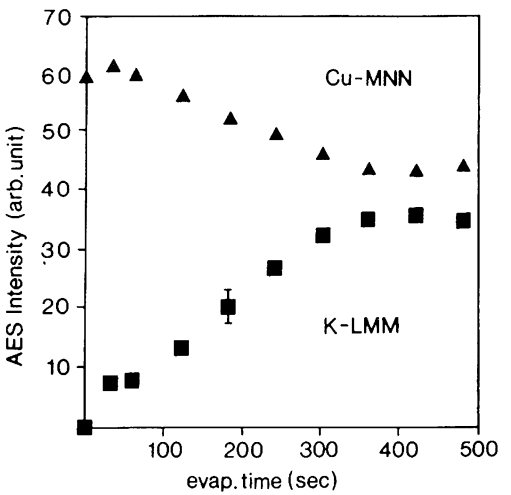

Fig. 2. AES peak to peak intensity of the Cu-MNN and the K-LMM transition versus K evaporation time. The saturation of the signals indicates the completion of one overlayer corresponding to a coverage of about 0.35–0.37 ML.

Using this roughness model the intensity distribution along the CTR can be written as:

$$I = |F_{hkl}|^2 g(h)g(k) \frac{1}{4\sin^2 \pi l} \frac{(1-\beta)^2}{[1+\beta^2-2\beta\cos(\pi l)]}. \tag{3}$$

III. Measurements

The measurements were carried out at the beamline X 16A of the National Synchrotron Light Source (NSLS) storage ring of the Brookhaven National Laboratory (BNL) using a UHV diffractometer (Fuoss and Robinson, 1984) in the five circle diffraction geometry described in detail by Vlieg, Van der Veen, MacDonald and Miller (1987).

The Cu(100) surface was prepared under UHV conditions (base pressure 10^{-10} mbar) by 30 min or Ar^+ ion sputtering (500 eV) at a sample temperature of $T = 800$ K followed by 5 min annealing at $T = 730$ K. The sample heating was achieved by electron bombardment. Within the detection limit of the Auger electron spectrometer the Cu(100) surface was clean. A low background LEED pattern could be obtained.

The potassium atoms were deposited from thoroughly outgassed SAES dispensers at a sample temperature of $T = 330$ K. The calibration of the evaporation rate was performed by Auger electron spectroscopy. In Fig. 2 we show the evolution of the potassium-LMM (252 eV) and the copper-MNN (60 eV) Auger peak to peak signals versus evaporation time. The saturation of the signals is well known as an indication of the completion

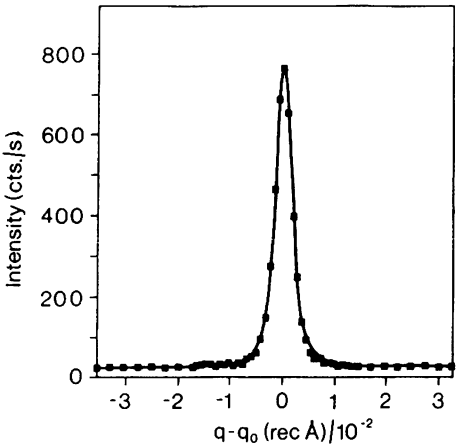

Fig. 3. Representative transverse scan (ω-scan) over the $(10\ 0.1)_t$ reflection corresponding to the antiphase condition midway between the $(101)_t$ and the $(10\bar{1})_t$ Bragg points (see Fig. 1). The width of the reflection curve reflects the sample mosaic of about 3.8 $\times 10^{-3}$ Å^{-1} corresponding to 0.3°.

of one potassium layer on the Cu(100) surface corresponding to about Θ = 0.35 to 0.37 ML (Aruga et al., 1985).

For the X-ray measurements the Cu(100) sample was aligned using the bulk $(101)_t$ and $(10\bar{1})_t$-Bragg peaks. Using a Si(111) double crystal monochromator the beam energy was set to E = 8.73 keV corresponding to λ = 1.42 Å. This is slightly below the Cu-K-edge (E_{CuK} = 8.98 keV) and far above the potassium K-edge ($E_{K.K}$ 3.61 keV).

Slits of 2×10 mm were mounted 500 mm behind the sample providing a longitudinal resolution of 2.4×10^{-3} Å^{-1}. The resolution parallel to the truncation rods is 1.4×10^{-2} Å^{-1}, corresponding to about 0.05 reciprocal lattice units. The measurements were transverse scans by rotating the crystal around the surface normal (ω-scan). The Fig. 3 shows a representative reflection curve at $(10\ 0.1)_t$ versus ω. In the transverse direction the resolution is limited by the sample mosaic spread which in the present case is about $\Delta\omega = 3.8 \times 10^{-3}$ Å^{-1} corresponding to 0.3° FWHM. Although the reflection $(10\ 0.1)_t$ corresponds to the out-of-phase condition the intense primary beam provides a high signal to noise ratio. The measured peak intensity is about 800 counts per second. Larger momentum transfers $q_z = l \cdot c^*$ were attained at constant beam exit angle β_f = 3° by rotating the whole diffractometer table around the α-axis (Vlieg et al., 1987) thereby increasing the X-ray incidence angle β_i. The integrated intensities along the rod were measured in steps of $\Delta l = 0.2$. In Fig. 4 the filled squares indicate the integrated intensities measured along the $(10l)_t$-rod of the clean Cu(100) sample after correcting the data for the active sample area as well as for

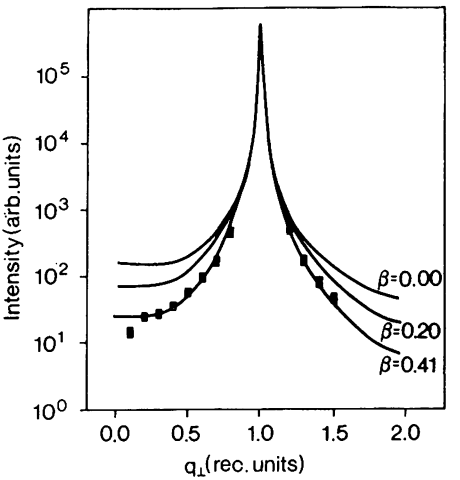

Fig. 4. Integrated intensity along the $(10l)_t$ rod of the uncovered Cu(100) surface (filled squares) compared with several simulations taking the surface roughness into account (solid lines). The error bars corresponds to about the size of the symbols.

the Lorentz- and the polarization-factor (Feidenhans'l, 1989; Robinson, 1991, 1992). Several symmetry equivalent reflections have been measured, the reproducibility was about 5–10%. The measurement of one rod took about $1^1/_2-2$ h depending on the primary beam intensity. Afterwards the first scan of the whole run has been repeated in order to check the reproducibility of the measurements and the stability of the structure. In most cases the reproducibility was within one standard deviation of the counting statistics. Additionally, it should be noted that contamination might be less important when investigating the local adsorbate geometry only and not the superstructure which requires a well defined long range order.

Using Eq. (3) we have fitted the data along the $(10l)_t$-rod shown as solid lines. In order to fit the data far off the $(101)_t$-Bragg peak the roughness parameter β was set to 0.41 which corresponds to a root mean square asperity height of the surface of $\sigma_{rms} = 2.1$ Å, which is in the range normally seen for metal surfaces (Robinson, 1986).

In order to elucidate the effect of the surface roughness we have additionally plotted the calculated rod intensities for $\beta = 0.0$ and $\beta = 0.20$. The influence of the surface roughness is most prominent at the out of phase condition between the Bragg-peaks, whereas the curves converge close to the Bragg-peak.

IV. CTR-analysis of K/Cu(100)

After measuring the CTR-intensities of the clean Cu(100) surface in the first experiment about 0.14 ML potassium were evaporated and the data acquisition was repeated immediately using the identical diffractometer settings used for the measurement of the uncovered sample.

In Fig. 5 the squares represent the ratios between the integrated intensities of the potassium covered and the uncovered sample for the $(10l)_t$ and the $(20l)_t$ rod. The adsorbed potassium atoms modulate the CTR intensities by up to 30%. The analysis of the intensity ratio is considerably more accurate than considering the measured intensities only, since the geometric correction factors cancel. The adsorbed potassium atoms are taken into account by coherently adding their scattering amplitude to the scattering amplitude of the underlying bulk substrate crystal. The total intensity is given by:

$$I(hkl) = \left| \frac{f_{Cu}(1 + e^{i\pi(h+k+l)})}{1 - e^{-i2\pi l}} + f_K \Theta_K e^{i2\pi(hx+ky+lz)} \right|^2 . \quad (4)$$

The first term represents the scattered amplitude of the clean Cu(100) sample. The structure factor F_{hkl} of the unit cell is given by the numerator, where f_{Cu} is the atomic scattering factor of Cu. In the second term f_K and Θ_K represent the scattering factor of potassium and the coverage, respectively. The factor exp $[i2\pi(hx + ky + lz)]$ contains the information about the potassium adsorption site given in fractional coordinates (x, y, z) within the unit cell. From this it can be seen that besides the determination of the alkali adsorption height, $d_\perp = z \cdot c_0$, the analysis of the $(10l)_t$ rod allows to distinguish between high symmetry sites such as fourfold hollow- $(x = 1/2, y = 1/2, z)$, on-top- $(x = 0, y = 0, z)$ and the bridge sites $(x = 0, y = 1/2, z)$, $(x = 1/2, y = 0, z)$. This is not possible using the $(20l)_t$ rod, where only the alkali adsorption height can be deduced.

In Fig. 5 the solid lines correspond to the calculated intensity ratios assuming $\Theta = 0.14$ ML potassium to be randomly adsorbed in the fourfold hollow sites at $d_\perp = 2.20$ Å ($z = 0.61$, $c_0 = 3.61$ Å) above the first Cu(100) layer. Additionally we allowed the substrate interlayer relaxation Δd_{23} to change from $\Delta d_{23} = +1.7\%$ reported for the uncovered sample (Davis and Noonan, 1983) to $\Delta d_{23} = 0$ upon potassium adsorption. The interlayer relaxation Δd_{12} was kept constant at $\Delta d_{12} = -1.1\%$. The values are given relative to the bulk layer spacing of $d = 1.808$ Å. Using these structure parameters for both data sets we obtain (unweighted) residuals of $R_u = 9.9\%$ and $R_u = 12.2\%$ for the $(10l)_t$ and the $(20l)_t$ rod, respectively.

The adsorbate structure is shown schematically in Fig. 6 illustrating the potassium and copper atoms as hard spheres. For comparison the effective atomic radii of copper and potassium as well as the effective ionic radius of potassium are shown (Pauling, 1960). Within the hardsphere model from

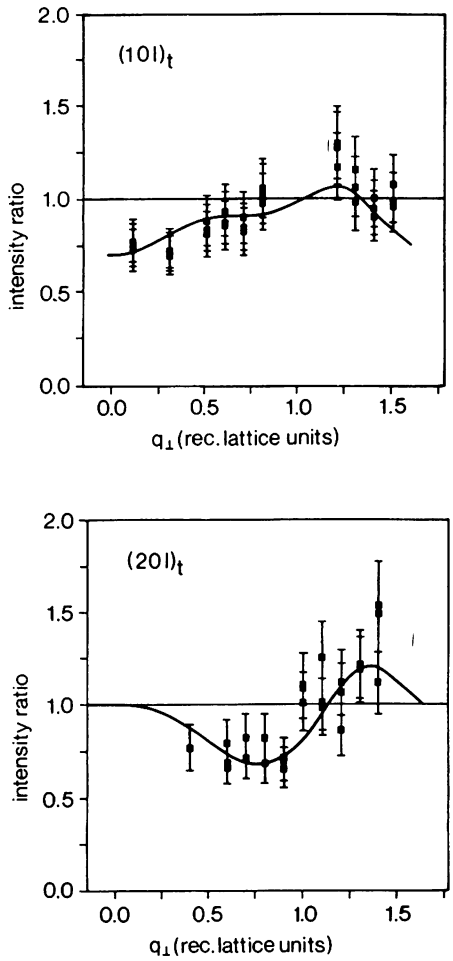

Fig. 5. Intensity ratios between the covered (0.14 ML) and the uncovered Cu(100) surface measured for the $(10l)_t$ and the $(20l)_t$ truncation rod. The solid lines correspond to calculations assuming adsorption of potassium in fourfold hollow sites at $d_\perp = 2.20$ Å above the first Cu layer. At large l the fits are slightly improved by assuming a change of the interlayer spacing d_{23} from $\Delta d_{23} = +1.7\%$ for the uncovered sample to $\Delta d_{23} = 0\%$ for the covered sample. The interlayer spacing d_{12} has been kept constant at $\Delta d_{12} = -1.1\%$. The values are given relative to the bulk spacing 1.808 Å.

$d_\perp$ the effective radius r_{eff} of the adsorbate can be evaluated provided that the radius of the copper atoms at the surface is given by the atomic radius of 1.27 Å.

We do not want to imply that the adatom charge distribution is spherical. However, the effective radius is useful for making bond length comparisons.

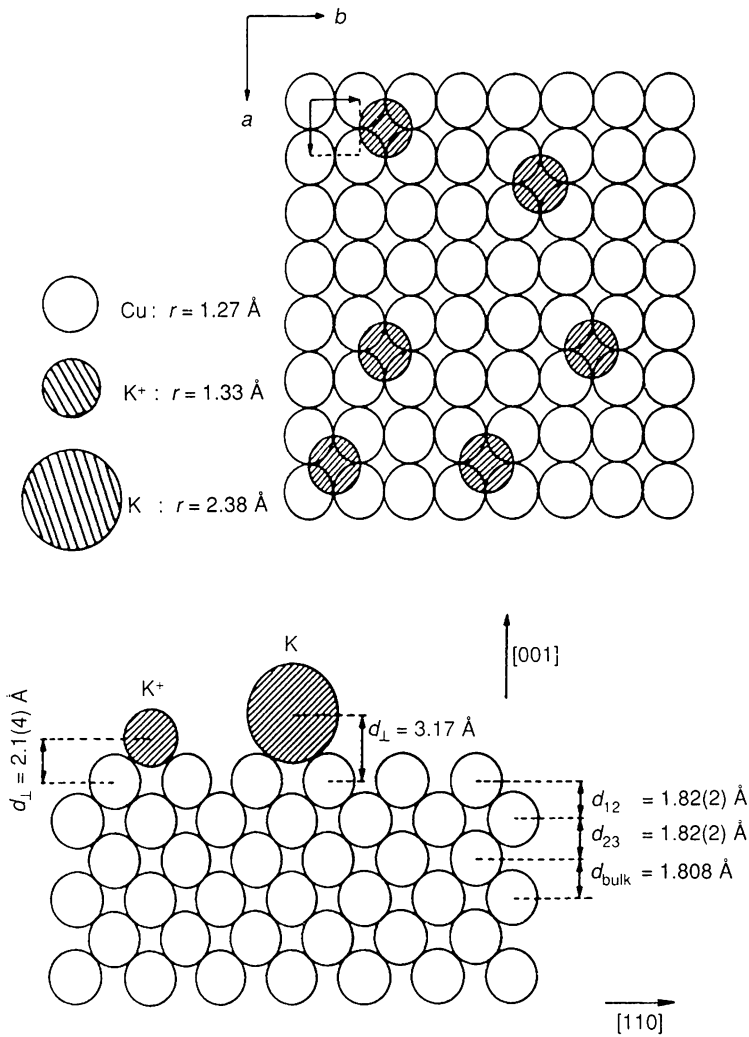

Fig. 6. Model of fourfold hollow adsorption of K on Cu(100) on top view (upper panel) and side view (lower panel) for about 0.14 ML coverage. The primitive surface unit cell is indicated in the upper left. The K atoms are assumed to be randomly dispersed over the surface due to mutual electrostatic repulsion. Within the hard sphere model the derived adsorption height $d_\perp$ = 2.1(4) Å corresponds to an effective potassium radius of 1.5(3) Å, close to the effective ionic radius (1.33 Å). Adsorption of atomic K gives $d_\perp$ = 3.17 Å which is far outside the error bars of the measurements. The interlayer spacings d_{12} and d_{23} are very little affected by K adsorption and nearly correspond to the bulk spacing.

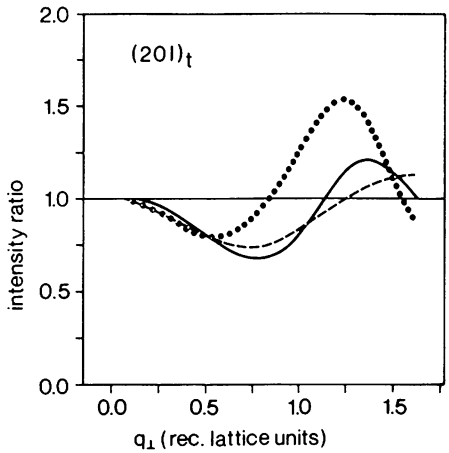

Fig. 7. Calculated intensity ratios for the $(20l)_t$ truncation rod. The solid line is identical with the fit shown in Fig. 5 corresponding to $d_\perp = 2.20$ Å, $\Delta d_{12} = -1.1\%$ and $\Delta d_{23} = 0\%$ for the covered sample. The dotted line represents the calculation using $d_\perp = 3.17$ Å corresponding to adsorption of atomic potassium in fourfold hollow sites (see Fig. 6). The alkali adsorption height can be estimated directly by the oscillation frequency (see text). The dashed line is calculated with the same parameters used for the solid line except $\Delta d_{23} = +1.7\%$ instead of 0%. Changing the interlayer relaxation upon potassium adsorption induces an asymmetry of the truncation rod intensity relative to the Bragg-points.

Using the fourfold hollow adsorption the agreement between experiment and simulation is reasonably well for both truncation rods. Note that at the Bragg-peaks $(101)_t$ and $(200)_t$ the intensity ratio must pass through the value $R = 1.0$, since all substrate layers scatter in phase and the effect of the potassium atoms becomes negligibly small.

Allowing for a variation of $d_\perp$ the agreement between experiment and calculation can be slightly improved for the $(10l)_t$ rod (optimum value $R_u = 8.0\%$ for $d_\perp = 1.90$ Å), however for $(20l)_t$ rod the agreement becomes worse. Additionally, including small changes of the interlayer spacings slightly improves both fits, especially at high q_z. For example, assuming no changes of d_{12} and d_{23} upon K adsorption leads to $R_u = 10.5\%$ for the $(10l)_t$ rod. We do not consider this as a clear indication for a change of the interlayer spacings.

The detailed consideration of all data set and the corresponding error bars lead to $d_\perp = 2.1(4)$ Å corresponding to $r_{\text{eff}} = 1.5(3)$ Å which is close to the effective ionic radius of 1.33 Å as shown in Fig. 6. If the potassium atoms were adsorbed with the atomic radius, the adsorption height would be 3.17 Å, far outside the error bar.

Increasing $d_\perp$ increases the oscillation frequency of the intensity ratio as a function of l due to the factor $e^{i2\pi lz}$. This is shown in Fig. 7 using the

$(20l)_t$ rod as example. The solid line represents the calculated intensity ratio shown previously in Fig. 5 assuming $d_\perp = 2.20$ Å, $\Delta d_{23} = 0$, $\Delta d_{12} = -1.1\%$ and $\Theta = 0.14$ ML ($R_u = 12.2\%$), whereas the dotted line is calculated for $d_\perp = 3.17$ Å keeping the other parameters constant. In this case the agreement with the experiment is much worse ($R_u = 24.8\%$).

The alkali height can be estimated directly from the curves by considering the position of the first minimum of the oscillations, l_{min} which corresponds to the antiphase condition of the adsorbate scattering amplitude, $e^{i2\pi lz} = -1$. Therefore, $z = 1/(2 \times l_{min})$.

For the solid line l_{min} is about 0.8 corresponding to $d_\perp = 2.25$ Å, whereas for the dotted curve we roughtly obtain from the plot $l_{min} \approx 0.55$ leading to $d_\perp = 3.28$ Å. It should be noted that simultaneous changes of the interlayer spacings have influence on the oscillations which are important at large l. This is illustrated by the dashed curve representing the intensity ratio for $d_\perp = 2.20$ Å and assuming no changes of the interlayer spacings upon potassium adsorption. Stated differently, the difference between the dashed and the solid curve is the value for d_{23} after potassium adsorption. It is 1.839 Å for the dashed curve ($R_u = 14.5\%$) and 1.808 Å for the solid curve ($R_u = 12.2\%$). The interlayer relaxation generally induces an asymmetric modulation of the truncation rod intensity relative to the Bragg points (Robinson, 1991). However, the modulation is only important at large momentum transfers $q_z = l \cdot c^*$ and is confined to about 10–15% if reasonable relaxations $|\Delta d| \approx 1-2\%$ are assumed. Nevertheless, taking into account the substrate relaxation may be important to fit the data correctly at large l. For this reason the determination of $d_\perp$ from the intensity oscillations is at least influenced at $l < 1$ (see Fig. 7) but this may seriously limit its accuracy.

One more parameter to consider is the coverage Θ which is linear in the scattered amplitude. From the AES measurements Θ is calibrated and is therefore fixed within 10–15%. The effect of increasing (decreasing) Θ is to increase (decrease) the amplitude of the oscillations around the ratio $R = 1$.

In order to fit the experimental data all these parameters can be continuously varied, where the calculated intensity ratio linearly responds to the variation. However, changing the lateral adsorption site has a dramatic effect on the intensity ratio for the $(10l)_t$ rod. In Fig. 8 we show as filled squares the measured $(10l)_t$ intensity ratio of $\Theta = 0.30$ ML potassium evaporated on Cu(100). Additionally we have plotted as solid line the calculated intensity ratio assuming *on-top* adsorption ($x = 0$, $y = 0$, z) at $d_\perp = 2.40$ Å and allowing for an 1% expansion of d_{12} and d_{23} relative to the bulk ($R_u = 13\%$). In contrast to the fourfold hollow site adsorption we observe at low l an increase of the scattered intensity relative to the uncovered sample.

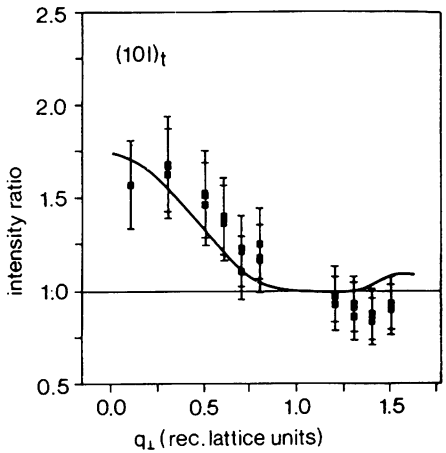

Fig. 8. Measured $(10l)_t$ truncation rod intensity ratio for about 0.3 ML potassium on Cu(100) relative to the uncovered sample. The solid line is a fit assuming on-top adsorption at $d_\perp = 2.40$ Å and $\Delta d_{12} = \Delta d_{23} = 1-2\%$.

The differences between the calculated intensity ratios for fourfold hollow- and on-top site adsorption can be understood in a straightforward way. We will explain this for one specific example: At $l = 0$ there is a phase shift of π between the scattering phases between fourfold hollow and on-top adsorption. From Eq. (4) follows that the amplitude F_{100} of the *uncovered* substrate is $f_{Cu}/2$. The perfect continuation of the crystal, i.e. "adsorption" of $\Theta = 1$ ML Cu in the fourfold hollow position (1/2, 1/2, 1/2) gives $I_{100} = |f_{Cu}/2 + f_{Cu}\, e^{i\pi(h+k+l)}|^2 = |f_{Cu}/2 - f_{Cu}|^2$ meaning that there is no change of the scattered intensity as expected. However, adsorption of $\Theta = 0.14$ ML potassium at (1/2, 1/2, 1/2) leads to $I_{100} = |f_{Cu}/2 - 0.14 f_K|^2$ corresponding to a 30% intensity reduction if the scattering factors for the (100) reflection, $f_{Cu} = 23.7$ and $f_K = 13.9$, are taken into account (Cromer and Waber, 1974).

On the other hand the adsorption of about 0.30 ML potassium at the on-top site (0, 0, z) gives $I_{100} = |f_{Cu}/2 + 0.30\, f_K\, e^{i2\pi lz}|^2 = |f_{Cu}/2 + 0.30\, f_K|^2$ which corresponds to an about 80% increase of the intensity relative to the uncovered sample. This is what we observe. In this context it is to note that at 0.30 ML we observed the formation of an ordered incommensurate overlayer structure between the commensurate phases labeled C1 and C2 by Aruga et al. (1985). Therefore the picture of potassium atoms occupying uniquely on-top sites is not strictly justified and for the detailed analysis a more sophisticated theoretical approach has to be applied which takes into account the modulation of the adsorbate layer (Toney, Gordon, Samant, Borges, Melroy, Kau, Wiesler, Yee and Sorensen, 1990). This will be discussed in a separate paper.

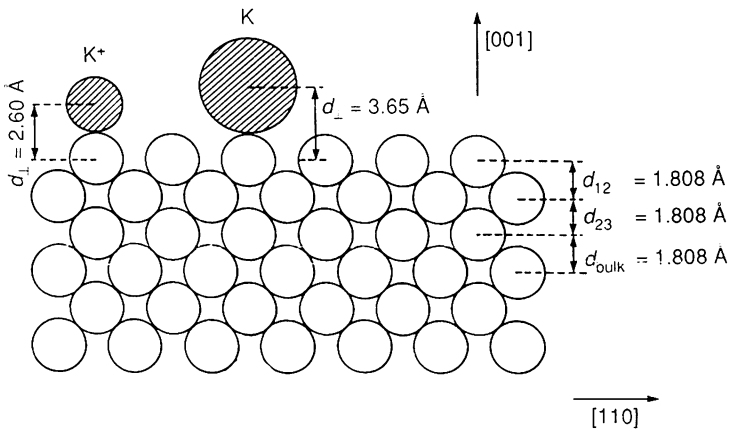

Fig. 9. Schematic view of the on-top adsorption site. The minimum adsorption height is $d_\perp$ = 2.60 Å assuming a covalent copper and a ionic potassium effective radius.

Nevertheless, the change of the scattering phase of the adsorbate relative to the substrate is a clear indication for the adsorbate changing site from fourfold hollow at low coverage to partially on-top at high coverage.

The on-top site is schematically illustrated in Fig. 9. Taking into account the radii of copper and of potassium (Pauling, 1960; Somorjai and Van Hove, 1979) the minimum adsorption height is $d_\perp$ 2.60 Å corresponding to the sum of the covalent copper and the ionic potassium radius. This is not in contradiction with the determined adsorption height $d_\perp$ since the latter value represents an average over different sites.

Besides the fourfold hollow and the on-top sites we considered different adsorption sites such as bridge sites ($x = 0, y = 1/2$), ($x = 1/2, y = 0$) as well as substitutional adsorption. None of them could be correlated with any of the experimental data.

Lateral relaxations of substrate atoms next to the adsorbate were additionally included into the calculations. A significant influence on the calculated intensity ratios was only observable assuming lateral shifts larger than about 0.1 Å. Consequently, this value represents an upper limit.

Finally, the observed intensity modulations cannot be explained by an increase of the surface roughness only, since this would lead to an intensity reduction on both sides relative to the Bragg-peak (see Fig. 3). In the present case we have assumed that the surface roughness is not influenced by the potassium adsorption.

V. Discussion and conclusions

In the previous section we have shown that potassium atoms adsorbed on Cu(100) in the coverage regime below 0.18 ML occupy fourfold hollow

sites at about $d_\perp = 2.1(4)$Å above the first Cu(100) layer. The application of the hard sphere model leads to an effective potassium radius $r_{eff} = 1.5(3)$ Å. This result suggests that the potassium atoms are adsorbed with an effective charge of almost $+1$. Within our experimental accuracy the substrate interlayer spacings are almost not influenced by the potassium adsorption. This is in agreement with other investigations (e.g. Over et al., 1992; Muschiol et al., 1992; Eggeling et al., 1989).

The model of the atomic structure discussed in the previous section is consistent with investigations performed so far on the electronic structure of low coverages of alkali metals on metal substrates. Present models (Aruga et al., 1984, 1985, 1986) suggest that the potassium atoms are randomly dispersed on the Cu(100) surface due to their mutual repulsion resulting from their partial positive charging.

Generally, the formation of ordered overlayers is influenced by the interplay between the adsorbate-adsorbate and the adsorbate-substrate interaction. Depending on the relative strength of these interactions AM/metal adsorbate systems are known to form commensurate and incommensurate phases, the latter only at high coverages close to the completion of a full monolayer, where a metallized alkali layer has been formed (Bonzel, Bradshaw and Ertl, 1989). In this coverage regime the adsorbate-adsorbate interaction tending to form close packed hexagonal layers dominates over the adsorbate-substrate interaction trying to pull the adsorbate atoms into high symmetry sites.

In contrast, at very low coverages the Coulomb interaction between the positively charged ions maximizes the mutual distance between the adsorbate atoms and the corrugation of the substrate potential determines sorption site which usually are sites with high coordination. In Table 1 we have summarized the results of previous investigations on AM adsorption on metals which are mostly confined to LEED investigations on ordered superstructures above $\Theta > 0.2$ ML.

At first it is to note that in all cases AM adsorbed on fcc (100) surfaces occupy fourfold hollow sites (Ref. b, g, k, l). On the other hand recent investigations have determined "unusual" on-top sites for $p(2\times2)$ structures on (111) surfaces (Ref. c, d, h) as well as a substitutional mechanism (Ref. m).

Over et al. (1992) suggest at $\Theta = 0.25$ ML the on-top site to be favored over the hollow site due to a more effective screening of the dipole-dipole repulsion between the adatoms by one substrate atom located directly between the adatoms. The same mechanism applies for the hcp threefold hollow site adsorption observed at $\Theta = 0.33$ ML. The inherently less favorable top site may become preferred due to the dipole screening. In this context the knowledge about the degree of charge transfer is highly desirable.

Table 1. Previous structural determinations for alkali metal adsorption on unreconstructed metallic surfaces.

System	Cov. (ML)	Site	Method	r_{eff}	r_{ion}	$r_{met.}$	Ref.
Cs/Ag(111)	0.15	–	SEXAFS	1.76(3)	1.67	2.68	(a)
Cs/Rh(100)-$c(4\times2)$	0.25	Hollow	LEED	2.10(6)	1.67	2.68	(b)
Cs/Ru(0001)$p(2\times2)$	0.25	Top	LEED	1.90(8)	1.67	2.68	(c)
Cs/Cu(111)$p(2\times2)$	0.25	Top	LEED	1.73(5)	1.67	2.68	(d)
Cs/Ag(111)	0.30	–	SEXAFS	2.06(3)	1.67	2.68	(a)
Cs/Ru(0001) $(\sqrt{3}\times\sqrt{3})$ R30°	0.33	Hollow	LEED	2.17(2)	1.67	2.68	(c)
Cs/Rh(100) $(\sqrt{5}\times\sqrt{5})$ R arc tan 0.5 – 2 Cs	0.40	Hollow and Top	LEED	2.12	1.67	2.68	(e)
Cs/Rh(100) $c[2\sqrt{2}\times2\sqrt{(2/3)}]$R45°	0.43	Incomm.	LEED	2.20	1.67	2.68	(e)
K/Cu(100)	0.14	Hollow	X-RAY	1.5 (3)	1.33	2.38	(f)
K/Ni(100)$c(4\times2)$	0.25	Hollow	LEED	1.96(5)	1.33	2.38	(g)
K/Ni(111)$p(2\times2)$	0.25	Top	LEED	1.57(3)	1.33	2.38	(h)
K/Co(100)$c(2\times2)$	0.50	Hollow	LEED	1.87(5)	1.33	2.38	(i)
Na/Ni(100)$c(2\times2)$	0.25	Hollow	LEED PED	1.59(10)	0.97	1.91	(k)
Na/Al(100)$c(2\times2)$	0.25	Hollow	LEED	1.43(7)	0.97	1.91	(l)
Na/Al(111) $(\sqrt{3}\times\sqrt{3})$ R30°	0.33	Subst.	SEXAFS	1.88(3)	0.97	1.91	(m)

[a] Lamble et al. (1989)
[b] Eggeling et al. (1989)
[c] Over et al. (1992)
[d] Lindgren et al. (1983)
[e] Besold et al. (1987)
[f] present work
[g] Muschiol et al. (1992)
[h] Fisher et al. (1992)
[i] Barnes et al. (1991)
[k] Demuth et al. (1975); Smith et al. (1980)
[l] Hutchins et al. (1976)
[m] Schmalz et al. (1991)

Valuable informations about the charge transfer is provided by the analysis of the effective adsorbate radius as a function of coverage. One should keep in mind that when considering the system of effective radii always the coordination number has to be taken into account. It is well known that, for ionic bonding, a decrease of the coordination number from 4 [fourfold hollow on (100)] to 3 [hcp-threefold hollow on (111)] to 1 (on-top) results in a decreasing effective radius by about 0.1 Å and 0.4 Å, respectively (Kittel, 1986).

Therefore the effective radii derived for the systems $c(4\times2)$K/Ni(100), $p(2\times2)$K/Ni(111) and $c(2\times2)$K/Co(100) [1.96(5) Å, 1.57(3) Å and 1.87(5) Å] are in agreement if the results are properly corrected for the coordination. This applies for the Cs and Na adsorbate systems as well.

As a result of the considerations we can state that there is a tendency for an increasing effective radius with increasing coverage. The only measurements performed so far on AM/metal systems at coverages lower than

0.20 ML, namely Cs/Ag(111) investigated by Lamble et al. (1988) using SEXAFS and the present work on K/Cu(100), reveal the lowest effective radii for the adsorbed alkali atom, which are close to the effective ionic radii. In contrast, the effective radii derived at coverages $\Theta > 0.2$ ML are halfway between the ionic and the metallic radii or even closer to the metallic radii. Lamble et al. additionally observe an increase of r_{eff} by 0.3 Å with increasing coverage, however, they were not able to derive the adsorption sites.

The second result of our investigations is the observation of the potassium atoms changing site from fourfold hollow at $\Theta \leq 0.18$ ML to partially on-top at $\Theta \approx 0.30$ ML. In order to explain this observation we may speculate that due to the metallisation of the overlayer the lateral adsorbate-adsorbate interaction dominates over the adsorbate-substrate interaction making the substrate corrugation potential less important for the hollow site occupation.

However, more information about the overlayer structure requires the analysis of the spatial modulation of the adsorbate layer. This will be discussed in a separate paper.

VI. Summary

We have shown how X-ray scattering which usually is a bulk probe can be made surface sensitive by the measurement of the intensity variation along the diffuse rods normal to the sample surface which arise due to the termination of the crystal. The analysis of an adsorption site does not require the formation of an ordered overlayer structure provided equivalent sites are occupied.

The present structure analysis on the adsorption of K on Cu(100) below 0.18 ML gave evidence for the occupation of fourfold hollow sites at $d_{\perp} = 2.1(4)$ Å above the Cu(100) surface. Using the hardsphere model this corresponds to an effective radius of 1.5(3) Å for the K adsorbate which is close to the effective ionic radius of K (1.33 Å). This result strongly supports the charge transfer model of alkali adsorption at low coverages.

The comparison with previous structure analyses which are concerned with ordered overlayers only ($\Theta > 0.2$ ML) gives an indication for a coverage dependent effective adsorbate radius and confirms the model of charge back donation and overlayer metallisation above about 0.2 ML. After adsorption of about 0.30 ML potassium an incommensurate quasi-hexagonal overlayer forms that has been reported previously. We observed a tendency of the adatoms to occupy on-top sites which can be explained by the increased lateral adsorbate interaction which dominates over the substrate corrugation potential.

Acknowledgement. We (H. L. M. and V. J.) would like to thank the American Telephone & Telegraph Inc. for providing access to the beamline X16 A and their hospitality during our visit in Brookhaven. The support of this work by the Bundesministerium für Forschung und Technologie under grant No. 0464IAB8 is gratefully acknowledged.

Work at the NSLS is supported by the US Department of Energy under DE-AC 012-76CH0016. Partial support also came from the University of Illinois Materials Research Laboratory under DEFG02-91ER45439.

References

Andrews, S. R., Cowley, R. A.: Scattering of X-rays from crystal surfaces. J. Phys. **C 18** (1985) 6427–6439.

Aruga, T., Tochihara, H., Murata, Y.: Rotational epitaxy of chemisorbed potassium monolayers on Cu(001). Phys. Rev. Lett. **52** (1984) 1794–1797.

Aruga, T., Tochihara, H., Murata, Y.: Structure and transitions of potassium monolayers on Cu(001). Surf. Sci. **158** (1985) 490–496.

Aruga, T., Tochihara, H., Murata, Y.: Two dimensional condensation of potassium adatoms on Cu(100). Surf. Sci. Lett. **175** (1986) L 725–L 729.

Aruga, T., Tochihara, H., Murata, Y.: Valence electronic structure of potassium adsorbed on Cu(001) deduced from work function change and electron energy loss spectroscopy. Phys. Rev. **B 34** (1986) 8237–8245.

Barnes, C. J., Hu, P., Lindroos, M., King, D. A.: The surface structure of a c(2 × 2) K overlayer on Co(100). Surf. Sci. **251/252** (1991) 561–567.

Batterman, B. W., Cole, H.: Dynamical diffraction of x-rays by perfect crystals. Rev. Mod. Phys. **36** (1964) 681–717.

Besold, G., Schaffroth, Th., Heinz, K., Schmidt, G., Müller, K.: Structures and transitions of Cs monolayers on Rh(100): LEED study and model calculations. Surf. Sci. **189/190** (1987) 252–260.

Bonzel, H. P., Bradshaw, A. M., Ertl, G.: *Physics and Chemistry of alkali metal adsorption.* Material Science Monographs, Vol. 57. Amsterdam: Elsevier Publishing 1989.

Cromer, D. T., Waber, J. T.: Atomic scattering factors for X-rays. In: *International tables for X-ray crystallography* Vol. IV (Eds. James A. Ibers and Walter C. Hamilton) p. 71–147. Birmingham, England: The Kynoch Press 1974.

Davis, H. L., Noonan, J. R.: Multilayer relaxation in metallic surfaces as demonstrated by LEED analysis. Surf. Sci. **126** (1983) 245–252.

Demuth, J. E., Jepsen, D. W., Marcus, P. M.: Overlayer structure determination by LEED at low energies: Na on Ni(100). J. Phys. **C 8** (1975) L 25–L 30.

Eggeling, C. von, Schmidt, G., Besold, G., Hammer, L., Heinz, K., Müller, K.: Structure determination of c(4 × 2)Cs/Rh(100) by LEED. Surf. Sci. **221** (1989) 11–22.

Feidenhans'l, R.: Surface structure determination by X-ray diffraction. Surf. Sci. Reports **10** (1989) 105–188.

Fisher, D., Chandavarkar, S., Collins, I. R., Diehl, R., Kaukasoina, P., Lindroos, M.: Top site adsorption for potassium on Ni(111). Phys. Rev. Lett. **68** (1992) 2786–2789.

Fuoss, P. H., Robinson, I. K.: Apparatus for X-ray diffraction in ultra high vacuum. Nucl. Instrum. Methods Phys. Res. **222** (1984) 171–176.

Horn, K., Hohlfeld, A., Somers, J., Lindner, Th., Hollins, P., Bradshaw, A. M.: Identification of the s-derived valence-electron level in photoemission from alkali metal adlayers on aluminum. Phys. Rev. Lett. **61** (1988) 2488–2491.

Hutchins, B. A., Rhodin, T. N., Demuth, J. E.: Surface crystallography of the c(2 × 2) Na overlayer on Al(100). Surf. Sci. **54** (1976) 419–433.

Ishida, H.: Theory of the alkalimetal chemisorption on metal surfaces. Phys. Rev. **B 38** (1988) 8006–8012.

Ishida, H.: Theory of the alkalimetal chemisorption on metal surfaces. Phys. Rev. **B42** (1990) 10899–10911.

Kittel, C.: *Introduction to solid state physics*, 6th Ed. London: John Wiley & Sons, Inc. 1986.

Lamble, G. M., Brooks, R. S., King, D. A., Norman, D.: Determination of an adlayer bonding transition by surface extended X-ray absorption fine structure spectroscopy: Cesium adsorbed on Ag(111). Phys. Rev. Lett. **61** (1988) 1112–1115.

Langmuir, I., Kingdon, K. H.: Thermoionic phenomena due to alkali vapours. Phys. Rev. **21** (1923) 380.

Laue, M.: Die äußere Form der Kristalle in ihrem Einfluß auf die Interferenzerscheinungen an Raumgittern. Ann. Phys. **26** (1936) 55–68.

Lindgren, S. Å., Wallden, L., Rundgren, J., Westrin, P., Neve, J.: Structure of Cu(111)p(2 × 2)Cs determined by low energy electron diffraction. Phys. Rev. **B28** (1983) 6707–6712.

Muschiol, U., Bayer, P., Heinz, K.: LEED structure analysis of Ni(100)c(4 × 2)-K. Submitted to Surface Science.

Over, H., Bludau, H., Skottke-Klein, M., Ertl, G., Moritz, W., Campbell, C. T.: Coverage dependence of adsorption site geometry in the Cs/Ru(0001) system: A low energy electron diffraction analysis. Phys. Rev. **B45** (1992) 8638–8648.

Pauling, L.: *The nature of the chemical bond*, 3rd Ed. Ithaca: Cornell University Press 1960.

Riffe, D. M., Wertheim, G. K., Citrin, P. H.: Alkalimetal adsorbates on W(110): Ionic, covalent or metallic? Phys. Rev. Lett. **64** (1990) 571–572.

Robinson, I. K.: Crystal truncation rods and surface roughness. Phys. Rev. **B33** (1986) 3830–3836.

Robinson, I. K.: Surface Crystallography. In: *Handbook of Synchrotron Radiation, Vol. 3* (Eds. G. S. Brown and D. E. Moncton), p. 221–266. Amsterdam: Elsevier Publishing 1991.

Robinson, I. K., Smilgies, D.-M., Eng, P. J.: Cluster formation in the adsorbate induced reconstruction of the O/Mo(001) surface. Submitted to Physical Review B.

Schmalz, A., Aminpirooz, S., Becker, L., Haase, J., Neugebauer, J., Scheffler, M.: Unusual chemisorption geometry of Na on Al(111). Phys. Rev. Lett. **67** (1991) 2163–2166.

Smith, N. V., Farrel, H. H., Traum, M. M., Woodruff, D. P., Norman, D., Woolfson, M. S., Holland, B. W.: Photoelectron diffraction effects in core level photoemission from Na and Te atoms adsorbed on Ni(100). Phys. Rev. **B21** (1980) 3119–3130.

Somorjai, G. A., Van Hove, M. A.: Adsorbed monolayers on solid surfaces. In: *Structure and bonding, Vol. 38*. Berlin: Springer Verlag 1979.

Soukiassian, P., Riwan, R., Lecante, J., Wimmer, E., Chubb, S. R., Freeman, A. J.: Adsorbate induced shifts of electronic surface states: Cs on the (100) faces of tungsten, molybdenum and tantalum. Phys. Rev. **B31** (1985) 4911–4923.

Toney, M. F., Gordon, J. G., Samant, M. G., Borges, G. L., Melroy, O. R., Kau, Lung-Shan, Wiesler, D. G., Yee, D., Sorensen, L. B.: Surface X-ray scattering measurements of the substrate induced spatial modulation of an incommensurate adsorbed monolayer. Phys. Rev. **B42** (1990) 5594–5603.

Vlieg, E., Van der Veen, J. F., MacDonald, J. E., Miller, M.: Angle calculations for a five circle diffractometer used for surface X-ray diffraction. J. Appl. Crystallogr. **20** (1987) 330–337.

Wallden, L.: Surface photoelectric effect for thin metal overlayers. Phys. Rev. Lett. **54** (1985) 943–946.

Woratschek, B., Sesselmann, W., Küppers, J., Ertl, G., Haberland, H.: 4*s* valence level of adsorbed K atoms probed by metastable He deexcitation spectroscopy. Phys. Rev. Lett. **55** (1985) 1231–1234.